Finite Element Modelling Of Blade Thermoelastic Stress Analysis Results

Dr Paul A. Bonnet[1A], Dr A. Geoff Dutton[2A]
[1] p.a.bonnet@rl.ac.uk, Tel +44 1235 778 251, Fax +44 1235 446 863
[2] g.dutton@rl.ac.uk, Tel +44 1235 445 823, Fax +44 1235 446 863
[A] Energy Research Unit, Rutherford Appleton Laboratory, Science & Technology Facilities Council, Chilton, Didcot, OX11 0QX, UK – www.eru.rl.ac.uk

Thermoelastic stress analysis (TSA) is a non-destructive method that is used to assess structural stress. It is based on the ability to measure stress induced thermal emissions during cyclic loading with an infrared camera. It has potential applications for the monitoring of wind turbine blades certification tests. In this work, conducted as part of the UK SuperGen Wind consortium, finite element (FE) analyses are conducted to evaluate the potential correlation with TSA outputs. Such correlation of FE and TSA for composite blade structures is key for the interpretation of TSA results and thus for the application of thermoelasticity to wind turbine blades. A flexible parametric structural model for wind turbine blades is presented, based on a Python script and the ABAQUS solver. Typical wind turbine blade geometry, which can be tailored by the user, enables the generation of a regular mapped mesh. The application of industry standard materials and layups is also enabled, as well as various loading types. It is then shown through a particular case study using a 4.5m long blade that the main characteristic stresses of the loaded structure are reasonably well represented by both the FE and TSA techniques and that some manufacturing defects can be detected at an early stage by TSA measurements. This is encouraging and suggests that the use of TSA should be pursued by the wind energy sector.

1- Introduction

Thermoelastic stress analysis (TSA) is a non-destructive experimental method that is used to assess the stress distribution on the surface of a structural component. It is based on the ability to measure stress induced thermal emissions during cyclic loading through the use of an infrared camera. The TSA theory has been presented in numerous books and papers, such as [1], [2] and [3]. The main points are briefly exposed in section 2 of this paper. It has potential applications in the monitoring of wind turbine blade certification tests – for example to validate expected stress distributions or to reveal stress concentrations due to manufacturing defects.

Finite element (FE) analysis is now a mature procedure for the study of stress distribution in complex composite parts such as wind turbine blades. FE is well suited to examine particular phenomena or designs and, to some extent, potential alternative designs (see for instance [4], [5] and [6]). However, the cost in user time and effort in realising a full sensitivity analysis can be very high unless the analysis is parametric, which is not usually the case.

This work was carried out under the UK EPSRC Supergen Wind consortium, in which the main interest of the authors is to look at the constraints and possible solutions to the trend in increasing the size of future large wind turbine blades. The range of blade loading conditions and related requirements is large and their relative importance may vary (see [7] for a detailed discussion of blade loading). A fully parametric FE model for blade structures, particularly well suited to this framework, has been produced in the Python scripting language and implemented in the ABAQUS v6.7 commercial FE package. This model is presented in section 3 below.

In order to increase the confidence of using experimental TSA results, a case study is then presented based on experimental TSA data previously collected [8] during the fatigue test of a glass fibre reinforced plastic (GFRP) blade featuring shear-web and trailing edge debonds. The modelling of the defects is presented in section 4 and in section 5 the FE and TSA results are then compared.

2- TSA theory and its application to a wind turbine blade

The thermo-elastic stress analysis technique makes use of an infrared thermography camera. The general formulation for the thermo-elastic signal produced at the camera is given by Equation 1:

$$S = -\frac{eT}{DRG\rho c_p}\left(\alpha_{11}\Delta\sigma_{11} + \alpha_{22}\Delta\sigma_{22} + \alpha_{12}\Delta\sigma_{12}\right) \quad (1)$$

where e is the structural surface emissivity, T is the absolute temperature, D is the detector responsivity, R is a temperature correction factor, G is the amplification factor, ρ is the material density, c_p is its specific heat at constant temperature, α_{xx} are the coefficients of thermal expansion and σ_{xx} are the surface stress components in the directions indicated by the subscripts, and finally Δ represents variations over the testing range.

For isotropic and orthotropic materials, only the diagonal terms of the thermal expansion tensor are non-zero. In other words, α_{12}=0 and the shear stress component has no effect. The expression reduces to Equation 2:

$$S = -\frac{eT}{DRG\rho c_p}\left(\alpha_{11}\Delta\sigma_{11} + \alpha_{22}\Delta\sigma_{22}\right) \quad (2)$$

Equations 1 and 2 could be expressed in terms of principal stresses but this would involve knowing the coefficients of thermal expansion of the material in the directions of principal stress. Different areas of the structure having different principal stress directions, such an approach is not in general practical. Instead, using the blade main directions means that the coefficients of thermal expansion are in the longitudinal (0° for α_{11}) and transverse (90° for α_{22}) directions for the entire blade.

In practice, it is likely that the technique senses over a finite – very small – depth into the surface material. For the blade design used in this work, as is typical for many wind turbine blades, the most external laminate for the whole outer surface is a ±45° ply. The thermal expansion coefficients α_{11} and α_{22} for such a ply are necessarily equal, as long as the two directions are chosen to be orthogonal. Equation 3 follows, where the testing range variation Δ can now combine the sum of the stresses:

$$S = -\frac{eT\alpha}{DRG\rho c_p}\Delta\left(\sigma_{11} + \sigma_{22}\right) \quad (3)$$

It can be argued that the most external layer analysed by the infrared equipment is actually the surface layer composed by a film of epoxy resin only that inevitably covers any well wetted reinforced plastic structural component – note that the blades used in the experimental programme did not receive an external layer of gel-coat. The experimental data does not permit to draw any conclusion on this matter. The point made above about the thermal expansion coefficients still applies in the case of a film of resin, but its value α is different from that of the composite ply. Moreover, the values for e, D, ρ and c_p are also specific to the material being analysed. The resin layer, with its relatively poor mechanical properties, can be seen as a strain witness of the underlying fibre reinforced composite. The plane-stress state of this isotropic layer can be characterised by:

$$\begin{aligned}\sigma_{11} &= \frac{E}{1-\nu^2}\left(\varepsilon_{11} + \nu\varepsilon_{22}\right)\\ \sigma_{22} &= \frac{E}{1-\nu^2}\left(\nu\varepsilon_{11} + \varepsilon_{22}\right)\end{aligned} \quad (4)$$

Expressing the sum of the principal stresses as is relevant for the TSA output leads to:

$$\sigma_{11} + \sigma_{22} = \frac{E}{1-\nu^2}\left(1+\nu\right)\left(\varepsilon_{11} + \varepsilon_{22}\right) \quad (5)$$

Thus, to a scaling factor, an isotropic strain witness such as a resin or gel-coat layer at the outer surface of the composite structure can also be regarded as a TSA output witness. This statement has been validated computationally in the FE model where no significant difference could be observed.

Consequently, the FE analysis stress output will be summed and scaled into a signal *A* according to Equation 6:

$$A = K\Delta(\sigma_{11} + \sigma_{22}) \quad (6)$$

where *K* is an arbitrary proportionality factor taking into account the equipment related terms and the material related terms. Thanks to the scaling factor, Equation 6 applies regardless of whether the sensed material is the composite or a surface strain witness layer. The application of Equation 6 to the FE outputs will enable direct comparison with the thermoelastic stress distribution measured experimentally.

3- The parametric finite element model

A parametric and flexible modelling strategy is sought in order that the blade external geometry, internal structural shape, structural mesh, materials, loads, analysis type and post-processing operations can all be adjusted independently. This way, the model development time is optimised and a high proportion of the CPU usage time is spent producing results. Working with the commercial Abaqus FE solver, these specifications lead to the use of a Python script as the analysis definition core. All aspects of an analysis can be automated from within the script thanks to the comprehensive features of the Python programming language, augmented by additional functions available to control Abaqus.

Although the aerodynamic shape can be complex because it is based on non-planar surfaces, a complete geometry is defined by way of a fairly simple topology. As shown in Figure 1, the outer shape can be defined by consecutive 2D sections (e.g. circle at the root and specific aerofoil profiles at the other sections) and a list of distances from root to tip where each section is present. This volume is further adapted by other user inputs for each section, such as chord lengths, twist angles, thickness scaling, pitch axis location, etc. The complete aerodynamic surface is then defined by an interpolation process creating a smooth surface through the successive curves. A natural cubic spline algorithm is used in the code developed. The production of the surface (and later the mesh) within the script means that a computer aided design package is totally unnecessary in the analysis loop.

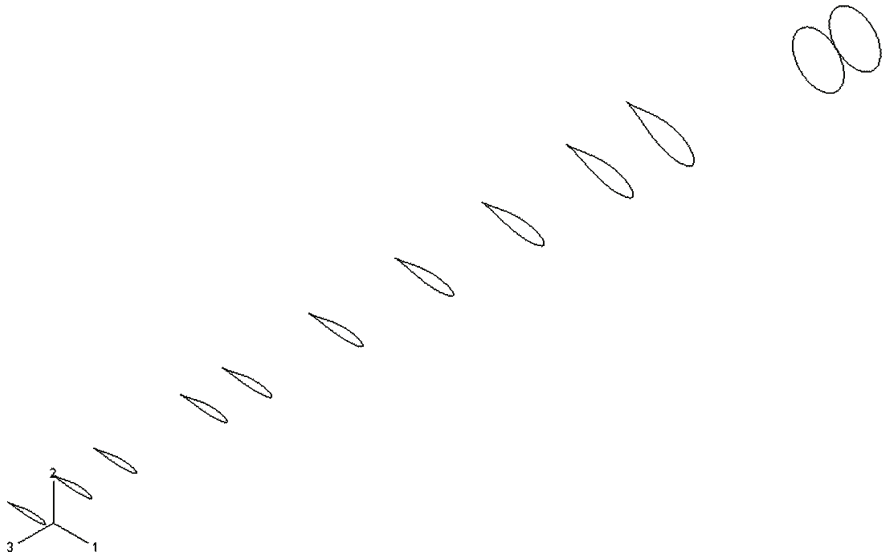

Figure 1: External surface topology

The general structural modelling principle is articulated around the definition of zero-thickness shells for the main composite structural elements (aerodynamic surfaces and internal shear-webs) and 3D brick volumes for the adhesive joints used to connect the composite parts. Two internal shear webs are defined parametrically by stipulating the distances from root where they start and end as well as their transverse positioning. The four glue layers are inserted between the shear-web flanges and the outer skins; the glue thickness is also defined parametrically in the script. Figure 2 shows the layout of the internal structure.

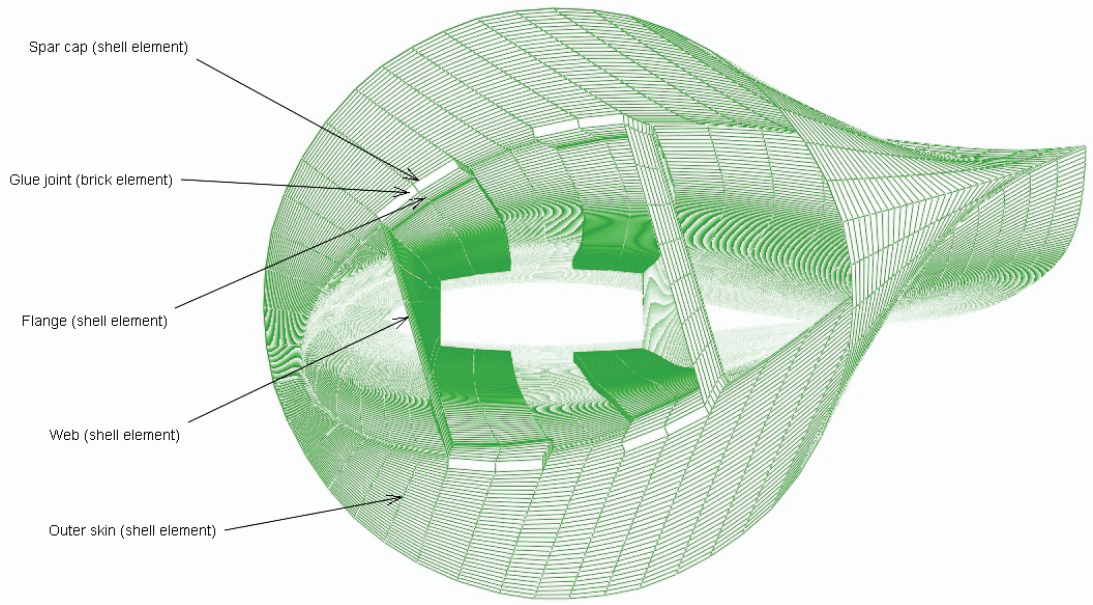

Figure 2: Typical mesh produced by the script and imported into Abaqus

From this geometrical definition, and using the cubic spline algorithm mentioned above, a fully structured mesh is generated numerically and is input into the ABAQUS environment (as shown in Figure 2). This strategy of generating the mesh independently from any third party geometry and mesh builder has several benefits. No geometry entity needs to be defined in Abaqus. The whole model is defined as a series of nodes and elements – the nodal coordinates are calculated from the user-defined geometry parameters and desired element sizes. The total control over the meshing algorithm enables a fully structured mesh to be created and the mesh connectivity between the various sub-components is produced automatically. To replace the presence of geometry entities used for the application of materials and boundary conditions, a list of element and node sets is defined. The structured character of the mesh and the data structure in Python largely facilitate these operations.

The script also gives the user the choice of using linear (S4R shells and C3D8R bricks) or quadratic elements (S8R shells and C3D20R bricks). The linear and quadratic shells in Abaqus have slightly different behaviours. The linear S4R element is a general-purpose shell while the quadratic S8R features a thick-shell approximation and a constant thickness. As in this application, this is likely to be excessive in most wind turbine blade designs. Linear shells were used in this study.

The blade structural characteristics are described through the input of specific data for the materials and layups used. Glass fibre reinforced plastic (GFRP) components are used in this study. Such composites are modelled as orthotropic laminar sections, giving characteristics in the main two directions. A composite layup can then be defined, composed of a succession of plies, each based on a particular GFRP material and aligned relatively to the main directions of the blade. In the layup, each ply can be related to a specific region of the mesh. The whole blade is covered by four layups – one for each outer skin side and one for each shear-web. Figure 3 shows a layup implemented in Abaqus.

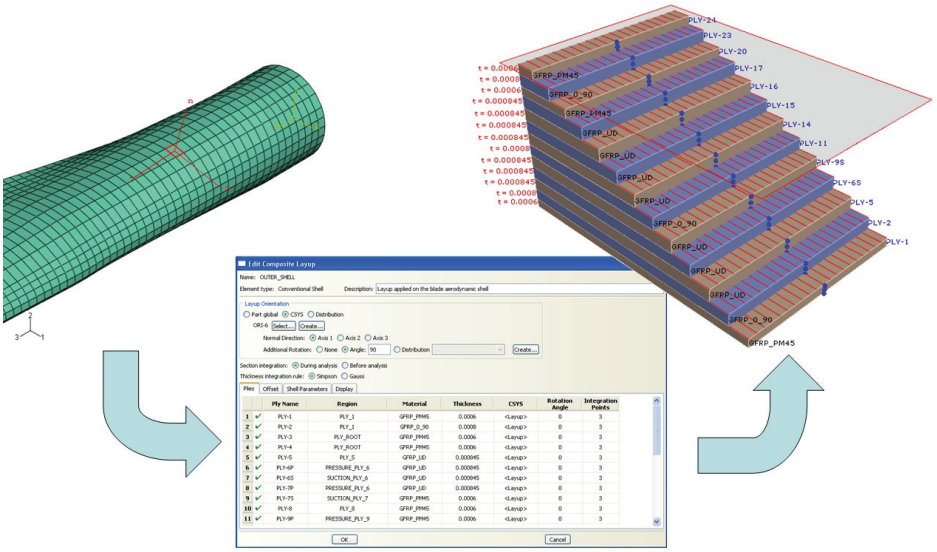

Figure 3: Application of a composite layup in Abaqus

Another user parameter provides for the possibility of taking into account non-linear geometric effects. This is necessary when large deflections occur or, for instance, in the case of modelling the centrifugal stiffening. Non-linearity is used for the present study due to the nature of the TSA measurements. The experimental results were obtained through recording over sinusoidal loading cycles of 0.3kN-3.0kN peaks at 1Hz, with the load input at a single section 3m from the root. The load range expressed is therefore 2.7kN, but it could be argued that FE results from a single 2.7kN analysis might be different from the subtracted results between separate analyses at 0.3kN and 3kN. The implementation of non-linear geometrical behaviour makes this problem irrelevant and the difference between the two loading peak output data will be produced.

One key aspect in realistic structural modelling of wind turbine blades is the accuracy of the loading conditions, which come from numerous sources. Pure strength under extreme loads, fatigue strength under operational loads and tip/tower clearance all bring specific design requirements. The increase in diameter also makes the rotor and blade mass related requirements more severe. It is again in the interest of the researcher to make these load models parametric as part of the script, in order to minimise the time spent as well as the possibility of introducing errors. A fully integrated aerodynamic loading procedure based on the potential flow theory around aerofoils and the blade element momentum theory is currently being implemented. The results presented in this paper, however, only make use of simple loads applied at a given blade section on the pressure side in the out-of-plane (flap) direction.

Analysis post-processing is also largely automated. Key results are output in a text file (e.g. deflections at the blade tip, total mass, sectional mass and stiffness properties, etc.) and Abaqus plots are produced and saved as images. Data manipulation is also enabled. For the TSA experimental data comparison, the variation over cyclic loading of the sum of the surface stresses in the two main blade directions is post-processed.

Finally, a sensitivity analysis functionality is built into the script to enable powerful design and scientific studies. This enables the tuning of any parameter used to create the model, including those that affect the blade internal and/or external geometry. This is also fully automated as an additional outer loop and does not require user intervention between consecutive runs. For FE analyses, this tool is initially practical for mesh convergence studies.

4- The blade model with artificial manufacturing defects

This study makes use of thermo-elastic stress analysis data collected during the EC Framework Programme 4 project *Acoustic emission proof testing and damage assessment of wind turbine*

blades (AEGIS) in which the principal objective was to develop a suitable methodology for the application of acoustic emission monitoring to wind turbine blades [8]. During this programme, ten blade tests were carried out on a set of nominally identical small (4.5m) blades (four with deliberately introduced flaws). Rutherford Appleton Laboratory applied the TSA methodology to two of these tests. The test of interest in this study was conducted on a blade which featured two artificially introduced manufacturing defects:

- trailing edge (TE) debond between *r*=900mm and *r*=1100mm,
- shear-web / skin debond between *r*=2000mm and *r*=2200mm on the compressive side of both shear-webs,

where *r* denotes the location distance from the blade root.

The data necessary to model the AEGIS blade was input into the parametric script and initial FE analyses were produced very quickly. The retained mesh has a nominal element length of 30mm. Due to the structured nature of the mesh, many elements are actually smaller – the nominal value is typically used around the root and maximum chord section. The material, section and layup data was also introduced. The structure is mainly composed of ±45°, 0/90° and uni-directional (UD) polyester GFRP laminates, 5mm glue joints, as well as 5mm and 10mm thick foam panels to create sandwich sections in the outer skins near the TE as well as in the webs. Also, a steel layer is included in the root area to simulate the presence of the steels studs used for fixing the blade to the turbine hub.

The defects were introduced in the FE model by disconnecting the elements located on either side of the debond, duplicating the nodes concerned and reconnecting the debonded elements with the new nodes as necessary. Note that the nodes located at the debond edges (i.e. at *r*=2000mm on the shear-web) were left unaffected. In total, 35 nodes were added to the blade model and 32 elements were reconnected.

The analysis of the defected model is carried out and it is checked that no connectivity is applied between the debonded areas. But even though a gap opens as and when expected, the shell elements that are no longer linked by common nodes can also cross over – i.e. the tensile side of the TE debond can displace through the compressive side and vice-versa. This behaviour is meaningless in real life and contact interactions are required to stop unrealistic motion and provide a sliding framework if required.

At this stage, the defect models are checked through post-processing of the longitudinal and transverse stresses in the structure. More precisely, it is possible to demonstrate that the defects introduce stress concentrations or discontinuities between the areas they separate. However, it should be remembered that there are layup discontinuities at *r*=1800mm and *r*=2300mm but none between *r*=2000mm and *r*=2200mm where the shear-web/skin defect is present. So any discontinuity observed at elements between *r*=2000mm and *r*=2200mm is purely due to the debond models. However, regarding the trailing edge debond, there is a layup discontinuity at *r*=1000mm, which will have to be taken into account when examining the results.

Firstly, the shear-web/skin debond is looked at from the shear-web perspective. Figure 4 presents the longitudinal stresses. It shows that discontinuities and compressive stress concentrations are manifest at the edges of the defects.

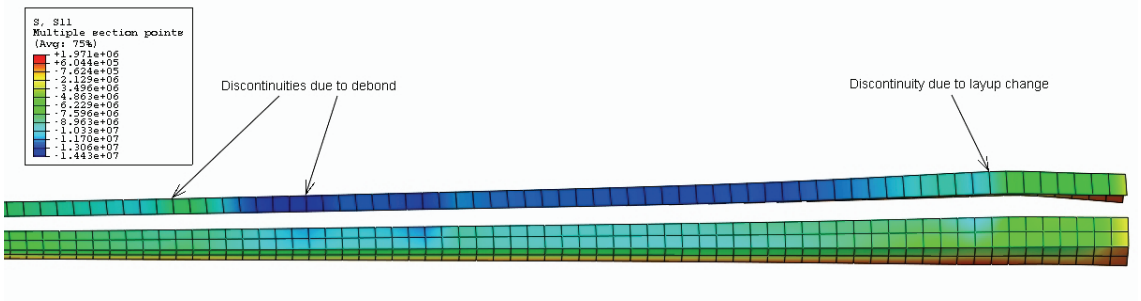

Figure 4: Longitudinal stresses on the compressive side flange of the shear-webs

When looking at the longitudinal stresses near the TE in the compressive skin, as shown on Figure 5, it is apparent that the TE defect results in stress concentrations at both “crack tips”. Part of the loading cannot transit through the edge and is therefore directed in the adjacent skin areas.

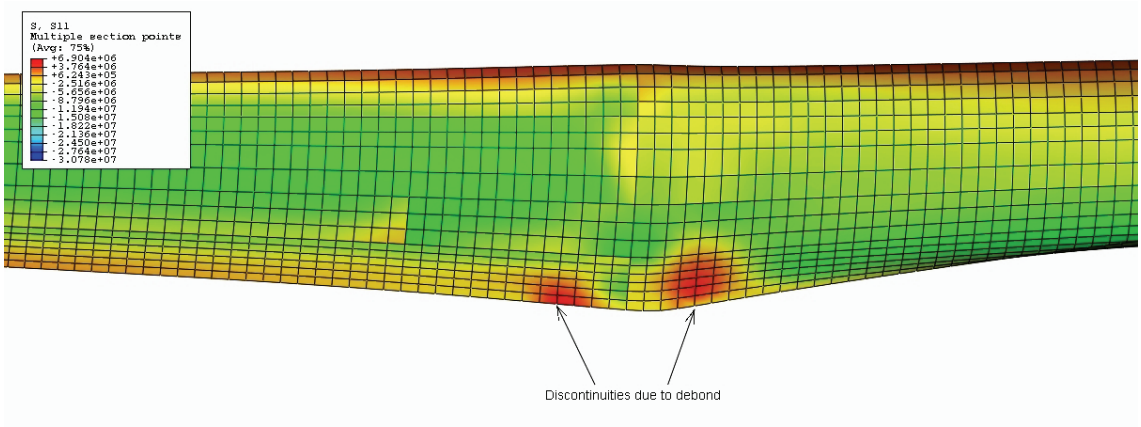

Figure 5: Longitudinal stresses on inner layer of compressive skin

As a further indirect check of the defects modelling validity, some general analysis results are given in Table 1 below for the following three analysis cases:

- Model 1: Initial model with no defect
- Model 2: With the TE and shear-web/skin elements disconnected
- Model 3: As above with the addition of contact elements between the disconnected elements

As would be expected, Table 1 shows that the blade model loses stiffness (deflection at loading point and natural frequencies) as the defects are first introduced to its structure (from Model 1 to Model 2). With Model 3 however most of this loss is regained, signifying that the inclusion of the contact interactions is crucial to realistic modelling.

	Model 1	Model 2	Model 3
Non-linear bending deflection (mm)			
0.3kN max deflection	20.03	20.42	20.05
3kN max deflection	200.2	204.1	200.4
Modal analysis frequencies (Hz)			
1st flap mode	5.686	5.650	5.685
2nd flap mode	15.12	15.10	15.12
3rd flap mode	36.02	35.85	36.02
1st edge mode	10.83	10.75	10.83
2nd edge mode	40.53	40.44	40.52

Table 1: Main results from modelling of the defects

5- Case study – TSA output from FE analysis

Results from the second test on a blade manufactured with the defects presented in section 4 are considered here. A bespoke Deltatherm infrared camera was used during the initial part of a fatigue test. Figure 6 shows the experimental setup, featuring a curtain to limit the amount of light reflection reaching the camera sensor. Figure 7 shows the graphical output, composed of 8 individual shots. The first 2.5m of the blade are shown, with the root on the right hand side (dimensions shown in mm). Note that the blade was also equipped with acoustic emission sensors (row of 4 on the ¼ chord line) and strain gauges (row of 4 black spots on spar cap with associated wiring to trailing edge) during the TSA measurements. These sensors exhibit a thermal behaviour of no comparison with the blade composites, resulting in excessive noise; the corresponding areas of Figure 7 should be ignored.

Figure 6: Experimental setup with TSA camera

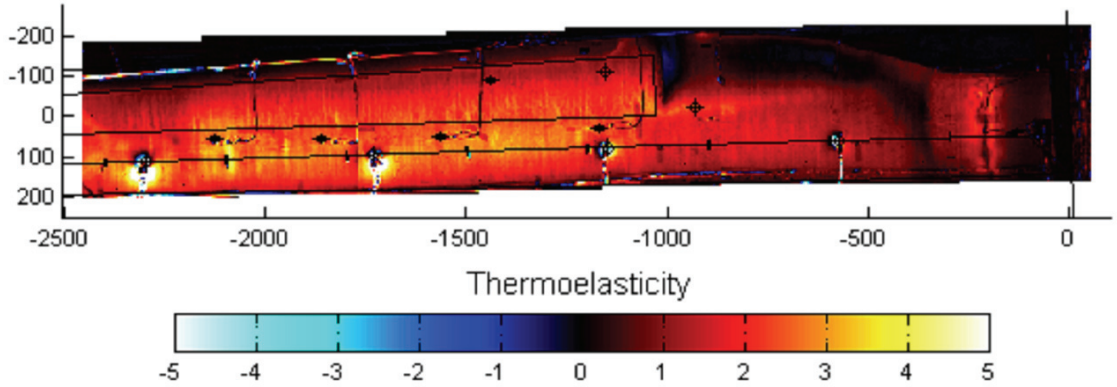

Figure 7: TSA experimental results of Aegis blade cyclic test at 0% life

From the FE model, a plot of the TSA output as expressed in Equation 3 is composed for the compressive side of the blade. This is presented in Figure 8. The FE results are scaled into the TSA output units and the relative results can be compared. The TSA signal results from the FE calculations are post-processed with an averaging method that does not take the layup region boundaries into account – see Figure 8. This reflects the results more accurately and Figure 8 should ultimately be compared with the experimental results of Figure 7.

Figure 8: TSA results from the FE model of the defected blade

By comparing Figures 7 and 8, the general agreement between the two solutions is confirmed. The relevance of the negative (blue) signal reaching the TE at the maximum chord section can be checked. Also, the positive (red) spot on the TE shown by the arrow on Figure 8 at *r*=900mm (please refer to Figure 7 for radial coordinate location) can also be seen on both solutions, inboard of which another larger area of negative signal extends. The neutral output at the root is likely caused by the steel present in the blade for the hub connection.

The light orange area extending from *r*=1200mm and *r*=2200mm between and close to the shear-web flanges is also replicated in the computational solution. Another noteworthy area from the computational point of view is that extending between *r*=700mm and *r*=1100mm along the TE shear-web, on the TE side. This orange strip is not as bright in the experimental results, even though a corresponding patch of lighter red/orange can be discerned. Overall, the broad agreement of the results should be stated.

As mentioned in section 2, given the uncertainty as to the material layer actually analysed by the TSA sensing equipment, a separate modelling analysis was conducted with an extra coat of polyester resin added to the outer skin blade layup. However, no difference with the results obtained without the additional resin could be seen. This confirmed the theoretical conclusions reached earlier.

The effects of the debonds on the TSA output results is also studied. Although no TSA data is available for a non-defected blade, FE outputs confirm that some defects could be detected early during a fatigue test. Figure 9 presents the TSA output from the FE analysis for the non-defected blade model. Comparing the fields presented in Figures 8 and 9 can therefore provide conclusions about the influence of the defects on the TSA output.

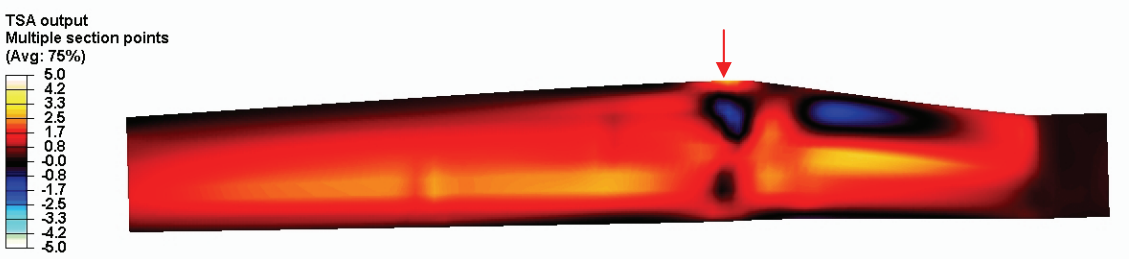

Figure 9: TSA results of the non-defected blade

The TE debond has a clear influence: the negatively marked area near the TE at the maximum chord section (*r*=1000mm) shown by the arrow on Figure 9 expands significantly to the TE in Figure 8, exactly where the defect is located. This graphical impact of the defect is in accordance with what can be seen from the experimental data of Figure 7.

However, the shear-web/skin debond is affecting the surface stresses much more subtly, and little or no impact can be detected by comparing Figure 8 and 9 only.

Conclusions

In this paper, finite element analysis has been used to compare results from experimental thermoelastic stress analysis results on the compressive side of a 4.5m wind turbine blade. The theory behind the application of TSA to wind turbine blades was presented. A parametric FE model developed for generic blade modelling was also described. The model was then modified to include some manufacturing defects. Finally, a comparative analysis was carried out between the results from the FE model and experimental TSA measurements.

All the main features observed from the experimental data are reproduced in the FE output: the main compressive loading area along the shear-web/skin connection and the relatively unloaded trailing edge alongside, the tensile area around the trailing edge debond at the point of maximum chord, and the generally neutral output observed at the root section due to the hub connection reinforcements. The TE defect could clearly be seen from the experimental data and it could be concluded that such defects could be filtered through systematic TSA monitoring. However, no clear signal could be observed regarding the shear-web. Overall, the results provide good indications that FE analysis and TSA results correlate reasonably well for complex GFRP blade structures with damage.

More work in this area is necessary. Notably, it should be assessed how deep into the structural surface the TSA equipment senses, especially with composite structures covered with a layer of gel-coat, typical of the wind turbine blade industry. Also, work on the application of TSA for the condition monitoring of blades when coming out of the factory would be necessary, ideally in collaboration with a blade manufacturer.

On the modelling front, future work will be conducted regarding the automation of loading conditions, including representative aerodynamic loads, centrifugal effects and gravity. Future studies will include looking at large blade size limits and potentially related design alternatives. Work regarding the structural dynamics aspects of complete machines will also be performed.

References

1. Stanley P, Chan, WK. The application of thermoelastic stress analysis to composite materials. *Journal of Strain Analysis* 1988; 23, 137-143.
2. Harwood N, Cummings WM. *Thermoelastic stress analysis*; Hilger, 1991.
3. Dulieu-Barton JM, Stanley P. Development and application of thermoelastic stress analysis. *Journal of Strain Analysis 1998;* 93-104.
4. de Goeij WC, van Tooren MJL, Beukers A. Implementation of bending-torsion coupling in the design of a wind-turbine rotor-blade. *Applied Energy* 1999; 191-207.
5. McKittrick LR, Carins DS, Mandell J, Combs DC, Rabem DA, Van Luchene D. Analysis of a composite blade design for the AOC 15/50 wind turbine using a finite element model. *Sandia National Laboratories Report* 2001; SAND2001-1441.
6. Jensen FM, Falzon BG, Ankersen J, Stang H. Structural testing and numerical simulation of a 34m composite wind turbine blade. *Composite Structures* 2006; 52-61.
7. Burton T, Sharpe D, Jenkins N, Bossanyi E. *Wind energy handbook*; Wiley, 2001; 219-293.
8. Dutton AG. Thermoelastic stress measurement and acoustic emission monitoring in wind turbine blade testing. *European Wind Energy Conference London* 22-25 November 2004

Acknowledgements

The authors wish to acknowledge the support of the EPSRC for the Supergen Wind Energy Technologies Consortium, grant number EP/D034566/1.
We are also grateful to Robert Paynter for the thermoelastic stress analysis measurements (EPSRC grant number GR/N04997/01) collected during the Aegis project (EC contract number JOR3-CT97-0283) and to the STFC's e-Science department for the computing resource facilities provided for running the finite element software.